

## Internal Molecular Conformation of Organic Glasses: A NEXAFS Study

Amara Zuhaib and Stephen G. Urquhart\*

Department of Chemistry, University of Saskatchewan, Saskatoon, SK, Treaty Six Territory,  
Canada S7N 5C9

### Abstract

The origin of the exceptional stability of molecular glasses grown by physical vapour deposition (PVD) is not well understood. Differences in glass density have been correlated with thermodynamic stability for thin films of *N,N'*-Bis(3-methylphenyl)-*N,N'*-diphenylbenzidine (TPD) grown by PVD at specific substrate temperatures below the glass transition temperature. However, the relationship between the internal conformation of glass molecules and thermodynamic properties of the molecular glasses is not well studied. We use carbon 1s near edge X-ray absorption fine structure (NEXAFS) spectroscopy to examine different TPD sample preparations in which differences in thermodynamic stability of the glass are known. DFT simulations of the NEXAFS spectra of TPD allow us to attribute spectroscopic differences to changes in the internal conformation of the TPD molecule and relate this conformation to the stability of the TPD glass. This provides a direct experimental measurement of the internal conformation of molecules forming an organic glass.

\* Corresponding author, [Stephen.urquhart@usask.ca](mailto:Stephen.urquhart@usask.ca)

## I. Introduction:

Glasses are non-equilibrium materials that can be formed by cooling liquids below their melting point, where crystallization is avoided during the cooling process. Organic glasses have been subject to strong research interest, as physical vapor deposition (PVD) was shown to prepare organic glasses with exceptional thermal stability.<sup>1-3</sup> These PVD-grown organic glasses have a higher density,<sup>4-7</sup> more efficient molecular packing,<sup>8-10</sup> and a lower enthalpy<sup>1, 8, 11, 12</sup> and heat capacity<sup>13</sup> than liquid cooled glasses. Other characteristics of PVD-grown organic glasses include an increased resistance towards water uptake<sup>14</sup> and a thermal expansion coefficient 3-14% lower than that of ordinary glasses.<sup>4</sup> PVD-grown organic glasses show improved electrical performance in organic thin-film devices<sup>6</sup> and improved resistance to photodegradation.<sup>1, 7</sup> An ordinary glass would need to be aged for over a thousand years to prepare a material with the properties (density, stability, etc.) possible to obtain through PVD-growth.<sup>8</sup> A better understanding of the origin of the stability of these organic glasses could lead to better use of these materials in advanced organic electronic materials.<sup>15, 16</sup>

The origin of the exceptional stability of PVD-grown organic glasses has been the subject of intense investigation. The enhanced surface mobility of the molecules during PVD growth is believed to be an important factor for the glass stability; this mobility is related to the substrate temperature during deposition.<sup>8</sup> Stable glasses are formed when the substrate temperature is kept close to  $0.85 T_g$ , where  $T_g$  is the glass transition temperature of the liquid cooled glass.<sup>1</sup>

Enhanced surface mobility during deposition is expected to lead to a partial equilibration of molecules at the glass surface, before the deposit is buried by subsequent layers.<sup>17, 18</sup> This would result in a higher stability and density in these PVD-grown glasses.<sup>8, 1, 19, 20</sup> When deposition is

performed on a cold substrate, the reduced surface mobility causes the deposited molecules to stick without undergoing rearrangement, making lower density and lower stability glass films.<sup>21</sup> Deposition rate can also affect the stability and density of PVD-grown organic glasses.<sup>11</sup> When organic glasses were grown with a lower deposition rate, a decrease in fictive temperature ( $T_f$ ) and an increase in onset temperature ( $T_{\text{onset}}$ ) was observed, indicating increased kinetic stability with decreased deposition rate.<sup>22</sup> A slower deposition rate will give deposited molecules more time to explore lower energy configurations on the film surface before being covered by subsequent layers.<sup>8</sup> A comparison of PVD-grown organic glasses prepared at different deposition rates with ordinary glasses aged for a long period of time suggest that molecular rearrangement at the film surface during deposition is much more rapid than bulk rearrangements.<sup>8</sup>

The stability of PVD grown molecular glasses is also linked with preferential molecular orientation in some PVD-grown organic glasses,<sup>18, 23</sup> which suggests a relationship between the high kinetic stability and anisotropic molecular packing.<sup>22, 23</sup> Studies of PVD-grown organic glasses show a correlation between increased thermodynamic stability and higher film density.<sup>22,</sup>

24-26

Near edge x-ray absorption fine structure (NEXAFS) spectroscopy is sensitive to structure and bonding in organic molecules,<sup>27, 28</sup> molecular orientation,<sup>29-31</sup> some forms of intermolecular interactions,<sup>32</sup> and internal molecular conformation in conjugated molecules.<sup>33</sup> Bishop *et al.* used angle dependent NEXAFS spectroscopy with surface sensitive partial electron yield detection to examine the surface structure of liquid cooled glasses of posaconazole.<sup>34</sup> Linear dichroism in these spectra demonstrated that posaconazole molecules at the free surface of the liquid cooled glass are highly oriented.<sup>34</sup> NEXAFS spectra can be highly sensitive to internal molecular conformation, through extended  $\pi$ -conjugation.<sup>33, 35</sup> For example, Urquhart *et al.*<sup>33</sup> demonstrated

the sensitivity of NEXAFS spectroscopy to chain conformation and aggregation in poly(3-hexylthiophene-2,5-diyl) (P3HT).

In this work, we use NEXAFS spectroscopy to measure the internal molecular conformation of N,N'-Bis(3-methylphenyl)-N,N' diphenyl benzidine (TPD) within different sample preparations. This material has been extensively studied as a stable organic glass.<sup>23, 36</sup> Characteristic spectroscopic energy shifts and spectral broadening are used together with DFT simulations to determine the internal molecular conformations in TPD glasses.

## II. Experimental

### A. Sample Preparation

N, N'-Bis (3-methylphenyl)-N,N' diphenyl benzidine (TPD, 99%) was purchased from Sigma Aldrich and used without purification. Silicon monoxide coated transmission electron microscopy (TEM) grids (Ted Pella, USA) were used as substrates for PVD deposited TDP thin films. The formvar support layer was removed using chloroform solvent before deposition. Indium foil (5x5 square mm) was used as a substrate for examination of TPD in powder form. TPD thin films were grown by PVD on silicon monoxide coated TEM grids. Deposition occurred from a resistively heated tungsten boat, at pressures below  $10^{-7}$  torr. The film thickness and rate of the deposition were monitored with a quartz crystal microbalance, and a rate of 0.7 - 0.9 Å/s was used for all depositions. The total sample deposited thickness was 90 nm. The substrate temperature during deposition was held at specific temperatures from -11 to  $56 \pm 0.5$  °C with a Peltier thermoelectric module. The substrate temperature was measured with a thermistor, which provided feedback to a TC-48-20 thermoelectric temperature controller (TE Technologies Inc). Three films were prepared, with substrate temperatures during deposition of -11.0 °C, 25.0 °C and 56.0 °C. Taking the  $T_g$  for TPD as 330 K,<sup>36</sup> these deposition temperatures

correspond to  $0.79 T_g$ ,  $0.90 T_g$  and  $1.0 T_g$  when represented relative to the glass transition temperature. TPD powder samples were prepared by pressing the powder into clean indium foil surface.

### **B. X-ray Absorption Spectroscopy**

Scanning Transmission X-ray Microscopy (STXM) was used to acquire NEXAFS spectra for the PVD grown TPD films. Experiments were performed on the ambient STXM microscope at the Spectromicroscopy (SM) beamline (10ID-1) at the Canadian Light Source.<sup>37</sup> The beamline exit slits were set to 35 microns with low energy grating, which corresponds to resolving power ( $E/\Delta E$ ) of around 3000.<sup>37</sup> Left circularly polarized photons were used. The energy scale of spectra recorded on the SM beamline was determined by introducing CO<sub>2</sub> into the STXM microscope chamber with the TPD sample in place. The calibration of monochromator energy scale was based on the two vibronic peaks of gaseous carbon dioxide (CO<sub>2</sub>): carbon 1s  $\rightarrow$ 3s ( $\nu=0$ ) and carbon 1s  $\rightarrow$ 3p ( $\nu=0$ ) transitions in CO<sub>2</sub>, which were set to the literature values of 292.74 eV and 294.96 eV, respectively.<sup>38</sup> Carbon 1s NEXAFS spectra extracted from different sample regions in the STXM microscope are reported as optical density ( $OD = -\ln(I/I_0)$ ) versus energy, where  $I_0$  was taken through a broken window of the SiO coated TEM grid. The post-edge of background subtracted NEXAFS spectra were calibrated to the background subtracted atomic cross-section of carbon.<sup>39</sup>

Carbon 1s NEXAFS spectra of the TPD powder compound was recorded on the SGM beamline (11ID-1) at the Canadian Light Source in total electron yield (TEY) detection mode.<sup>40</sup> The beamline exit slit was set to 25 microns with the low energy grating, which corresponds to a resolving power more than 5000. TEY detection on the SGM was used because it was not possible to obtain a sufficiently thin samples of the powder for transmission measurements in the

STXM. TEY spectra were normalized by taking the ratio of the sample current ( $I$ ) and the gold reference current ( $I_R$ ), where the gold reference spectrum was acquired in a separate scan. The energy scale of the SGM spectrum of TPD powder was calibrated by shifting the carbon  $1s(C-H) \rightarrow \pi^*_{\text{Aromatic}}$  transition (at  $\sim 285.2$  eV) to match the energy of same band in the NEXAFS spectra of TPD thin films measured in the STXM, for which a precise gas phase calibration was obtained. Data presented below shows that the carbon  $1s(C-H) \rightarrow \pi^*_{\text{Aromatic}}$  transition energy does not vary between different sample preparations.

Spectral analysis was performed using aXis 2000<sup>41</sup> and spectra were plotted for presentation using OriginPro software package.<sup>42</sup> Fits to determine NEXAFS peak energies were performed using Sigmaplot v10.0,<sup>43</sup> and fits to characterize spectroscopic data as a plane (e.g.  $z = ax + by + c$ ) were performed with published python codes.<sup>44</sup>

### C. Computational Methods

DFT simulations were used to model how carbon  $1s \rightarrow \pi^*_{\text{Aromatic}}$  transition energies<sup>45</sup> vary with the internal molecular conformation, as determined by specific dihedral angles within the TPD molecule. The molecular structure of TPD (**Scheme 1**) shows the following variables: the angle of the terminal phenyl or tolyl groups ( $\nu_1$ ); the angle between the two phenyl rings comprising the biphenyl group ( $\nu_2$ ); and relative angle and planarity of the tertiary amine group ( $\nu_3$ ).

The equilibrium geometry of TPD and the geometry and total energy of TPD with varied geometries were obtained through geometry optimization with the program Gaussian 16<sup>46</sup> using density functional theory calculations with the MO62X model and the 6-31+G(d,p) basis set.

The equilibrium geometry was obtained from an unrestricted geometry optimization; no imaginary frequencies were found.

To examine the effect of internal molecular conformation, calculations were performed to determine the total energy with respect to phenyl group rotation. Dihedral angles  $\nu_1$  and  $\nu_2$  were fixed while all other structural variables were varied to minimize the total energy of the molecule. Calculations were performed with these dihedral angles varied as a set between  $20^\circ$  and  $70^\circ$  in  $5^\circ$  steps for the phenyl/tolyl dihedral angle ( $\nu_1$ ) and between  $20^\circ$  and  $90^\circ$  in  $5^\circ$  steps for the biphenyl dihedral angle ( $\nu_2$ ). Dihedral angles of less than  $20^\circ$  lead to unphysical results due to steric interference.

DFT simulations of NEXAFS spectra were obtained using the program deMon2k version 6.0.1<sup>47,48</sup> using the PBE functional. The transition potential (TP-DFT) method and the half-core-hole approximation to simulate the effect of the core hole.<sup>49</sup> Diffuse functions (IGLO-III)<sup>50</sup> and extensive augmentation (XAS-I)<sup>49</sup> were used for the core excited atom, and equivalent core potentials were used on all other atoms except hydrogen, which was a triple zeta basis function. Simulations were obtained for each carbon atom in the TPD molecule and summed to obtain an overall molecular NEXAFS spectrum.

### III. Results

Figure 1a (top) presents the carbon 1s NEXAFS spectra of a TPD thin film (prepared by PVD at  $0.79 T_g$ ) and TPD in powder form. The width of features in the NEXAFS spectrum of the powder are narrower on account of the higher resolving power of those data ( $E/\Delta E$  of 5000 versus 3000). Minor shape differences between these spectra are attributed to the difference in detection mode, as transmission detection has better fidelity to the absorption cross section than TEY detection. Figure 1b (bottom) presents a close-up of the  $\pi^*$  region of these NEXAFS spectra. The first band at  $\sim 285$  eV is assigned as the carbon  $1s(\text{C-H}) \rightarrow \pi^*_{\text{Aromatic}}$  transition, originating from phenyl ring carbon atom sites that have C-H bonding. The second band at

~286.2 eV is assigned as the carbon  $1s(\text{C-R}) \rightarrow \pi^*_{\text{Aromatic}}$  transition, where the “C-R” notation refers to the NEXAFS transition originating from phenyl ring carbon atom sites that are bonded to a substituent. Carbon  $1s(\text{C-R}) \rightarrow \pi^*_{\text{Aromatic}}$  transitions are shifted to higher energy on account of the inductive effect of the group bonded to the C-R site.<sup>51</sup> A small shift in the energy of the carbon  $1s(\text{C-R}) \rightarrow \pi^*_{\text{Aromatic}}$  band (e.g. C-R  $\pi^*$  band) is perceptible between the powder and thin film spectrum, while the carbon  $1s(\text{C-H}) \rightarrow \pi^*_{\text{Aromatic}}$  band (e.g. C-H  $\pi^*$  band) appears at nearly constant energy, albeit with energy resolution differences. We use the notation C-H/C-R  $\pi^*$  band to refer to the experimental peak, which can be formed from multiple carbon  $1s(\text{C-H/C-R}) \rightarrow \pi^*_{\text{Aromatic}}$  transitions.

Figure 2 presents the experimental carbon 1s NEXAFS spectra of a series of TPD thin film that were deposited onto substrates held at temperatures corresponding to 0.79  $T_g$ , 0.90  $T_g$ , and 1.0  $T_g$ . The full spectra (Figure 2a, top) are similar on account of the consistent thickness of the samples and the use of transmission detection. Figure 2b (middle) presents the carbon 1s NEXAFS spectra of the C-H and C-R  $\pi^*$  region, while Figure 2c (bottom) focuses on the small changes present in the C-R  $\pi^*$  band. The TPD film sample deposited onto a substrate at 1.0  $T_g$  has a broader C-R  $\pi^*$  band than that band in the spectra of samples deposited onto substrates held at 0.79  $T_g$  and 0.90  $T_g$ . As the apparent width and the energy of the C-R  $\pi^*$  band can be interpreted subjectively on the basis of data presentation, the results of Gaussian fits of this band are presented in Table 1. These fit data show that the film deposited at 1.0  $T_g$  has a broader C-R  $\pi^*$  band (0.572 eV) than the 0.79  $T_g$  and 0.90  $T_g$  samples (0.462 eV and 0.449 eV, respectively), and that the energy of this band appears at slightly lower for the sample deposited at 1.0  $T_g$  (286.120 eV) than in the samples deposited at 0.79  $T_g$  and 0.90  $T_g$  samples (286.130 eV and

286.133 eV, respectively); the latter difference is small relative to the estimated uncertainty (20 meV).

The difference in the C-R  $\pi^*$  band between the TPD thin film and TPD powder spectra is much larger; this band is narrower (0.358 eV compared to 0.449 - 0.572 eV) and shifted to higher energy (286.290 eV, from 286.120 - 286.133 eV) in the powder. The significance of these results will be discussed below.

DFT simulations of the NEXAFS spectra are used to understand how the spectra evolve with internal conformation, in particular the C-R  $\pi^*$  band. Figure 3 presents a simulation of the carbon 1s NEXAFS spectrum of TPD calculated by TP-DFT calculations. This simulation was performed with a representative fixed geometry ( $\nu_1 = 40^\circ$ ;  $\nu_2 = 30^\circ$ ;  $\nu_3 = 39^\circ$  that is similar to the calculated equilibrium geometry of TDP ( $\nu_1 = 39.9^\circ - 40.7^\circ$ ;  $\nu_2 = 38.0^\circ$ ;  $\nu_3 = 39.2^\circ - 39.6^\circ$ ). The individual atomic contributions of different chemical moieties in TDP (terminal phenyl, terminal tolyl, and central biphenyl group) are presented with different vertical offsets. This simulation is compared to a representative experimental carbon 1s NEXAFS spectrum of TPD, which is presented with a 1.5 eV energy shift to account for the well-known energy difference between experiment and calculation.

The TP-DFT simulation shows how the lower energy C-H  $\pi^*$  band ( $\sim 285.0$  eV) and the higher energy C-R  $\pi^*$  band arise from individual carbon 1s  $\rightarrow \pi^*$  transitions that reflect the local chemical environment of each carbon atom in the molecule. The experimental spectrum is broader than the TP-DFT simulation on account of the presence of vibronic character (e.g., carbon 1s( $\nu=0$ )  $\rightarrow \pi^*$ ( $\nu=1, 2$ , etc) transitions) that are not considered in the TP-DFT simulations. For comparison, references <sup>52</sup> and <sup>53</sup> present a discussion of vibronic effects in benzene<sup>53</sup> and polystyrene,<sup>52</sup> which have similar vibronic character as the phenyl and tolyl moieties in TPD.

While vibronic structure is significant in the C-H  $\pi^*$  band, the TP-DFT simulation in Figure 3 also shows the importance of small chemical shifts to the overall shape of this band.

The TP-DFT simulation also shows a series of carbon  $1s(\text{C-R}) \rightarrow \pi^*_{\text{Aromatic}}$  transitions attributed to different moieties bonded to the phenyl ring.<sup>51</sup> The shift in the carbon  $1s(\text{C-R}) \rightarrow \pi^*_{\text{Aromatic}}$  transitions due to phenyl-phenyl bonding in biphenyl group is relatively small, so the transitions for these sites appears within the C-H  $\pi^*$  band. There are two well separated C-R  $\pi^*$  features: one associated with C-R bonding of the biphenyl group to the amine group (bottom trace,  $\sim 287.45$  eV) and a second that is a degenerate combination of the C-R bonding of the tolyl/phenyl bonding to the amine group. The C-R  $\pi^*$  transitions associated with the amine group (e.g. C-R(N) sites) are well separated from the C-H  $\pi^*$  band and form the experimentally observed C-R  $\pi^*$  band.

The experimental NEXAFS spectra shown in Figures 1 and 2 show a small but distinct variation in the C-R  $\pi^*$  band between different sample preparations. We hypothesize that these shifts are due to changes in the internal conformation of the TPD molecule. Scheme 1 shows a series of likely conformational variables, where the TPD molecule can show conformational flexibility by rotation of the terminal phenyl or tolyl groups ( $\nu_1$ ), rotation of the biphenyl dihedral angle ( $\nu_2$ ) or rotation of the amine group ( $\nu_3$ ) plane. A comparison of DFT-calculations with solid-state NMR measurements of a melt-quenched TPD sample shows that the DFT-optimized structure reasonably reflects the TPD structure in the condensed amorphous state.<sup>54</sup> A comparison of XRD and NMR show considerable variability in the dihedral angles of the phenyl and tolyl rings in the solid state.<sup>55,54</sup> Variable temperature XRD shows that significant rotational movement of the terminal phenyl/tolyl rings persists down to 150 K.<sup>55</sup> Further, XRD and NMR results show that TPD amine group is planar.<sup>55,56</sup>

To examine the dependence of the C-R  $\pi^*$  band on the internal molecular conformation, DFT calculations were performed to examine the total energy of TPD as a function of the phenyl/tolyl substituent dihedral angles ( $\nu_1$ ) and the biphenyl dihedral angles ( $\nu_2$ ). The tertiary amine plane angle ( $\nu_3$ ) was not varied, as this tends to a consistent inclined position ( $\sim 39^\circ$ ). For reference, our geometry optimization calculations of TDP (unrestricted optimization, no imaginary frequencies) predict that the terminal phenyl/tolyl groups have dihedral angles ( $\nu_1$ ) in the range  $39.9^\circ - 40.7^\circ$ , the benzene rings in the central biphenyl group have the dihedral angle ( $\nu_2$ ) of  $38.0^\circ$ , and the tertiary amine groups ( $\nu_3$ ) are planar but rotated by  $\sim 39.2^\circ - 39.6^\circ$  with respect to the benzene ring of the biphenyl group.

This energy surface plot is presented in Figure 4. The minimum energy is observed for  $\nu_1 = 40^\circ$ , and  $\nu_2 = 40^\circ$ , which is consistent with the equilibrium structure calculation. There is a higher barrier to rotation of the phenyl and tolyl groups on account of steric interference from the tolyl's methyl groups. A wider variation in the biphenyl dihedral is possible in the TDP samples, while rotation of the terminal phenyl/tolyl groups will be more tightly circumscribed by the significantly higher slope of this energy surface.

The surface presented in Figure 4 shows the constraints in which molecular conformation can vary in the formation of the TPD glass. This energy plot does not account for intermolecular interactions in the molecular solid, as we expect that intramolecular interactions will also contribute to the structural landscape of molecular solids.

TP-DFT simulations were performed to explore the effect of this internal molecular conformation on the NEXAFS spectra of the TPD samples. Figure 5 presents the simulated carbon 1s NEXAFS spectra of TPD at a series of phenyl/tolyl dihedral angles ( $\nu_1 = 30^\circ, 40^\circ$  and  $50^\circ$ ; top, middle, and bottom set of traces) and then at a series of biphenyl dihedral angles ( $20^\circ \leq$

$\nu_2 \leq 60^\circ$ ). The energy of the C-H  $\pi^*$  band and the C-R(Me)  $\pi^*_{\text{Aromatic}}$  transitions are relatively consistent for these conformations. These data show clear shifts in the C-R(N)  $\pi^*_{\text{Aromatic}}$  transitions associated with phenyl/tolyl C-R(amine) bonding (indicated by an asterisk) and the C-R(N)  $\pi^*_{\text{Aromatic}}$  transitions associated with C-R(biphenyl-amine) bonding (indicated by a pound sign). The peak that arises from the C-R(N) sites on the phenyl / tolyl groups (\*) is more intense than that from the biphenyl C-R(N) sites (#) on account of the number of atoms in each site (4:2 ratio). Considerable variation in the energy of these C-R(N)  $\pi^*_{\text{Aromatic}}$  transitions as a function of  $\nu_1$  and  $\nu_2$  dihedral angles is observed.

To better illustrate the shifts in the C-R(N)  $\pi^*$  band as a function of molecular conformation, these transition energies are plotted as a function of  $\nu_1$  and  $\nu_2$  dihedral angle in Figure 6. The top pane of Figure 6 presents the energy of the carbon  $1s(\text{C-R(N)}) \rightarrow \pi^*_{\text{Aromatic}}$  transition originating on the biphenyl group C-R(N) atoms, and the bottom pane the energy of the carbon  $1s(\text{C-R(N)}) \rightarrow \pi^*_{\text{Aromatic}}$  transition originating on the terminal phenyl/tolyl C-R(N) atoms. In both cases, these energy surfaces are nearly planar, and were fit to the equation of a plane ( $z = ax + by + c$ ) using a python code.<sup>44</sup> The results of this fit are presented in Table 2. As shown by the slopes obtained from this fit, the biphenyl dihedral angle ( $\nu_2$ ) has a weaker effect on the C-R(N)  $\pi^*$  peak energies, in part from distance of this dihedral angle from the core excited atom sites.

#### IV. Discussion

The experimental results presented in Figures 1 and 2 show that the width and energy of the C-R(N)  $\pi^*$  band varies between different TPD sample preparations. Specifically, the C-R(N)  $\pi^*$  band appears at higher energy for the powder TPD sample, while the position and breadth of the C-R(N)  $\pi^*$  band varies modestly for TPD thin film deposited at different substrate temperatures. The C-R(N)  $\pi^*$  band is the narrowest in the TPD powder sample, then next narrowest for the

sample deposited with a substrate temperature of  $0.90 T_g$  and  $0.79 T_g$ . The width of the C-R(N)  $\pi^*$  band is somewhat broader in the TPD samples deposited at higher substrate temperatures of  $1.0 T_g$ .

We hypothesize that the differences in density observed between more stable glasses (which show greater density) and less stable glasses (which show lower density) are related to molecular packing, which is indirectly related to the internal conformation of the molecule. Our experimental approach is sensitive to internal molecular conformation, thus providing new experimental information on the structure of molecular glasses.

TP-DFT simulations show how the C-R(N)  $\pi^*$  band varies with the internal molecular conformation. In this regard, the narrower C-R(N)  $\pi^*$  band in the TPD powder and the  $0.90 T_g$  thin film sample is consistent with a narrower range of conformations of the TPD molecule, while the broader C-R(N)  $\pi^*$  bands for TPD samples deposited at higher substrate temperatures indicate a broader range of molecular conformations in these films. Nevertheless, the range of dihedral angles is not high.

The energy of the C-R(N)  $\pi^*$  band can be used to determine the internal molecular geometry of TPD. The sensitivity of NEXAFS to internal conformation is well known,<sup>35</sup> and recent studies using TP-DFT calculations have shown sufficient precision to extract structural information on the conformation of the P3HT chain with different degrees of regio-regularity and annealing.<sup>33</sup> Calculated carbon 1s  $\rightarrow \pi^*$  transition energies align well with experiment, once the fixed offset between calculated and experimental energy scales is accounted for. From this, the internal conformation can be extracted from measured transition energies. This approach is used here to measure the internal conformation of TPD in powder and thin film samples.

The offset between experiment and calculation is determined from the data in Figure 3. The ~285 eV (experimental energy scale) of the C-H  $\pi^*$  band does not vary appreciably with internal molecular conformation (per Figure 5), so it is used to align experimental and computational energy scales. As discussed above, the experimental C-H  $\pi^*$  band broadens to higher energy due to vibronic transitions, and perhaps broadened to a lesser extent due to nuclear motion effects (see ref. <sup>57</sup>). To avoid vibronic and possible nuclear motion broadening effects, we have aligned the experimental maxima – which corresponds to the adiabatic carbon 1s(C-H;  $v=0$ )  $\rightarrow$   $\pi^*_{\text{Aromatic}}(v=0)$  transition – to the maximum in the calculated C-H  $\pi^*$  band. Previous results from the high resolution carbon 1s NEXAFS spectra of polystyrene show that the maxima in experiment and calculation align;<sup>52</sup> we expect a similar alignment for other substituted benzene species.

An offset of 1.50 eV ( $\pm 0.05$  eV) is required to align these scales in Figure 3, where the uncertainty reflects the breadth of the C-H  $\pi^*$  band maxima. For clarity of the following analysis, we have recalibrated the calculated energy scales in Figure 6 and Table 2 to match the experimental energy scales by subtraction of 1.50 eV. These data show the predicted relationship between the C-R(N)  $\pi^*$  band energy and internal conformation, based on TP-DFT calculations. A quick review of the experimental data in Figures 3 and 5 shows a potential complication of this analysis: the C-R(N)  $\pi^*$  band consists of transitions from two different sites, and that the phenyl/tolyl C-R(N)  $\pi^*$  contributions are twice as intense as the biphenyl C-R(N)  $\pi^*$  contributions on account of the ratio of C-R(N) atoms (4:2). As shown in Figure 5, the C-R(N) contributions from these sites respond differently to changes in the TPD dihedral angles. As a starting point, we use the equations in Table 2 to calculate the carbon 1s(C-R(N))  $\rightarrow$   $\pi^*_{\text{Aromatic}}$  transition energies for the calculated equilibrium geometry of TPD ( $\nu_1 = 39.9^\circ - 40.7^\circ$ ;

$\nu_2 = 38.0^\circ$ ): the carbon 1s(C-R(N) phenyl / tolyl)  $\rightarrow \pi^*_{\text{Aromatic}}$  transition would appear at 286.18 eV and the carbon 1s (C-R(N) biphenyl)  $\rightarrow \pi^*_{\text{Aromatic}}$  transition at 286.00 eV (both on experimental energy scales). This is in good agreement with the experimental results for the C-R  $\pi^*$  band presented in Figure 2.

We can now use the equations in Table 2 to *predict* the dihedral angles in TPD, based on the measured C-R(N)  $\pi^*$  band energies. If we assume that **both** C-R(N)  $\pi^*$  transitions occur at the same energy (as tabulated in Table 2), then a direct solution for the angles  $\nu_1$  and  $\nu_2$  can be obtained. These results are presented in Table 3, with the uncertainty originating from the calibration energy scale calibration. These results are reasonable for the TPD thin film samples (dihedral angles of  $41.6 - 47.6^\circ$ ), which are somewhat higher than the calculated equilibrium values for TPD ( $\nu_1 = 39.9^\circ - 40.7^\circ$ ;  $\nu_2 = 38.0^\circ$ ). The TDP powder results are very different ( $\nu_2 = \sim 120^\circ$ ), suggesting that the two C-R(N) transitions do not occur at the same energy.

A closer examination of the C-R(N)  $\pi^*$  band for the  $0.79 T_g$  sample in Figure 2 suggests that this band may be split into two, with weaker lower energy component at 285.9 eV and a stronger higher energy component at 286.1 eV. We expect a 2:1 ratio between the phenyl / tolyl C-R(N)  $\pi^*$  band and the biphenyl C-R(N)  $\pi^*$  band, so the weaker peak could be attributed to the biphenyl C-R(N)  $\pi^*$  contribution. This is a suggestion, and beyond what can be reasonably claimed from the data. Using these energies in the equations in Table 2, we obtain dihedral angles  $\nu_1 = 48^\circ$  and  $\nu_2 = -3^\circ$ . This is close to an equilibrium  $\nu_1$  dihedral, and nearly planar for the biphenyl  $\nu_2$  dihedral. The range of biphenyl  $\nu_2$  dihedral results is not unreasonable, given the low barrier to rotation observed in Figure 4.

The difference between the TDP powder and thin film C-R  $\pi^*$  bands – and the predicted dihedral angles – are harder to rationalize. In truth, we know little about the structure of this TPD powder;

this is an ‘as received’ sample, following synthesis and purification by the chemical supplier’s contractor. The density of the powder form of TPD is known to be less than that of vacuum deposited TPD thin films (1.145 g/cm<sup>3</sup> for the powder; 1.153 g/cm<sup>3</sup> for thin film),<sup>25</sup> where increased density is correlated with increased stability. Taken with this density data, wider divergences in the dihedral angles are expected for *less stable* forms of TPD such as the powder sample.

The internal conformation of TPD is expected to be affected by molecular packing, arising from the PVD process. For vacuum deposited films, molecules on the surface are highly mobile and can reach a more stable configuration before being buried.

## V. Conclusions:

We have acquired the carbon 1s NEXAFS spectra of thin films of TPD prepared by PVD on substrates with temperatures ranging from -11 °C (0.79 T<sub>g</sub>) to 56 °C (1.0 T<sub>g</sub>) as well as a powdered PVD sample. Small but significant changes are observed in the C-R(N)  $\pi^*$  band in these spectra. TP-DFT calculations were used to explore the sensitivity of the C-R(N)  $\pi^*$  band to the internal molecular conformation in TPD. The calculations show a strong dependence of the C-R(N)  $\pi^*$  band energy on characteristic dihedral angles that define the internal conformation of TPD. As TP-DFT calculations have an excellent precision and reliable calibration for  $\pi^*$  transitions, the internal conformation of TPD was determined by combining experiment and theory. Our results show that the internal conformation of TPD in PVD deposited thin films is similar but slightly more twisted than that obtained from DFT calculations of an isolated molecule. The most stable TPD samples (prepared at 0.79 T<sub>g</sub> and 0.90 T<sub>g</sub>) have a smaller range of internal conformation dihedral angles, as shown by the narrower C-R(N)  $\pi^*$  band, as well as a decrease in the phenyl/tolyl rotation and an increase in the biphenyl rotation. The internal

conformation arises from the dynamics of molecular reorganization during deposition, and the increased density of the more stable TPD films relates to closer packing, either reflected by or facilitated by the changes in internal conformation of TPD in the glass.

### **ACKNOWLEDGMENTS**

SGU is funded by NSERC (Canada). This research was enabled in part by support provided by Westgrid and Compute Canada. NEXAFS spectra were acquired at SM and SGM beamlines at the Canadian Light Source, which is supported by the Natural Sciences and Engineering Research Council of Canada, the National Research Council Canada, the Canadian Institutes of Health Research, the Province of Saskatchewan, Western Economic Diversification Canada, and the University of Saskatchewan.

### **Data Availability**

The data that support the findings of this study are available from the corresponding author upon reasonable request.

**Scheme:**

**Scheme 1:** Schematic of the TPD molecule, with the terminal phenyl/tolyl ( $\nu_1$ ), biphenyl ( $\nu_2$ ) and amine plane ( $\nu_3$ ) dihedrals indicated.

**Figure Captions:**

**Figure 1. (a)** Carbon 1s NEXAFS spectra of different forms of TPD: TPD film prepared by PVD at 0.79 T<sub>g</sub> (black trace) and TPD powder (red trace), obtained with left circular polarized light. **(b)** Close-up of the NEXAFS spectra changes in carbon 1s  $\rightarrow$   $\pi^*$  region.

**Figure 2. (a)** Carbon 1s NEXAFS spectra of TPD films prepared by physical vapour deposition at different substrate temperatures: 0.79 T<sub>g</sub> (black trace), 0.9 T<sub>g</sub> (blue trace) and 1.0 T<sub>g</sub> (red trace), obtained with left circular polarized light. **(b)** Close up to show spectral changes in carbon 1s(C-H)  $\rightarrow$   $\pi^*$ <sub>Aromatic</sub> (C-H  $\pi^*$  band; 285 eV) and carbon 1s(C-R)  $\rightarrow$   $\pi^*$ <sub>Aromatic</sub> (C-R  $\pi^*$  band; ~286.2 eV) regions and **(c)** a close up of the carbon 1s(C-R)  $\rightarrow$   $\pi^*$ <sub>Aromatic</sub> (C-R  $\pi^*$  band; ~286.2 eV) region.

**Figure 3.** (bottom) TP-DFT simulations of the carbon 1s NEXAFS spectra of TPD at a selected geometry ( $\nu_1 = 40^\circ$ ;  $\nu_2 = 30^\circ$ ). Contributions from chemically inequivalent atoms in the terminal phenyl, terminal tolyl and central biphenyl groups are indicated by separate traces, as well as the total simulated spectrum (sum). (top) Experimental carbon 1s NEXAFS spectrum of a TPD thin film (deposited on a substrate at 25° C or 0.90 T<sub>g</sub>). The energy scale of these plots is offset by 1.50 eV to align the experimental spectra with the calculated data.

**Figure 4:** Calculated total energy of TPD as a function of the phenyl/tolyl dihedral angle ( $\nu_1$ ) and the biphenyl dihedral angle ( $\nu_2$ ). Energies were provided from DFT geometry optimization calculations with fixed dihedral angles, as described in the text.

**Figure 5.** (bottom) TP-DFT simulations of the carbon 1s NEXAFS spectra at a series of phenyl/tolyl dihedral angles ( $\nu_1 = 30^\circ, 40^\circ$  and  $50^\circ$ ) and biphenyl dihedral angles ( $20^\circ \leq \nu_2 \leq 60^\circ$ ). (top) Experimental carbon 1s NEXAFS spectrum of a TPD thin film (deposited on a substrate at  $25^\circ\text{C}$  or  $0.90\text{ Tg}$ ). The energy scale of these plots is offset by 1.50 eV to align the experimental spectra with the calculated data.

**Figure 6.** Energy of the carbon 1s (C-R)  $\rightarrow \pi^*_{\text{Aromatic}}$  transition for amine bonding sites on the biphenyl group (top) and phenyl/tolyl groups (bottom) as a function of biphenyl ( $\nu_2$ ) and terminal phenyl/tolyl dihedral angles ( $\nu_1$ ). The x-axis is set to match the experimental energy scale.

**TABLES:****Table 1:** Gaussian fits of the experimental C-R  $\pi^*$  band for TPD powder and TPD thin films.

TPD Sample	Fit Parameters <sup>a</sup>				
	Energy (eV) ( $x_0$ ) <sup>b</sup>	Width (eV) ( $2\sigma$ ) <sup>b</sup>	Pre-exponential factor (a)	Background ( $y_0$ )	R <sup>2</sup>
0.79 Tg	286.130	0.462	0.608	0.453	0.9847
0.90 Tg	286.133	0.449	0.666	0.462	0.9948
1.0 Tg	286.120	0.572	0.754	0.342	0.9721
TPD Powder	286.290	0.358	0.462	0.498	0.9903

- Sigmaplot (version 10.0)<sup>43</sup> was used to fit the C-R  $\pi^*$  band; band to a single Gaussian peak, using a four-parameter fit,  $f(x) = y_0 + a e^{-\frac{1}{2}\left(\frac{x-x_0}{\sigma}\right)^2}$
- The uncertainty in the energy positions and widths is estimated at 20 meV.

**Table 2:** Results of a fit to determine the parameters of a plane defining the energy of the Phenyl/tolyl C-R(N) carbon 1s(C-R)  $\rightarrow \pi^*$ <sub>Aromatic</sub> transition and the biphenyl carbon 1s(C-R)  $\rightarrow \pi^*$ <sub>Aromatic</sub> transition as a function of  $\nu_1$  (phenyl/tolyl dihedral angle) and  $\nu_2$  (diphenyl dihedral angle). A published python code was used for this fit.<sup>44</sup> The energy scale is set to match the experimental scale.

<b>Biphenyl carbon 1s(C-R(N)) <math>\rightarrow \pi^*</math><sub>Aromatic</sub> transition</b>
$z = 0.014414 (\nu_1) + 0.005216 (\nu_2) + 286.7182a$
<b>Phenyl / tolyl carbon 1s(C-R(N)) <math>\rightarrow \pi^*</math><sub>Aromatic</sub> transition</b>
$z = -0.009039 (\nu_1) + 0.000272 (\nu_2) + 288.0381^a$

- The energy scale has been recalibrated to the experimental energy scale by the subtraction of 1.5 eV.
- The energy scale accuracy is estimated as 20 meV

**Table 3: Calculation of Dihedral Angles – Single C-R  $\pi^*$  Energy Assumption**

Species	C-R energy (eV)	$\nu_1$ ( $^\circ$ ) <sup>a</sup>	$\nu_2$ ( $^\circ$ ) <sup>a</sup>
0.79 Tg	286.13	45.5 $^\circ$	46.2 $^\circ$
0.90 Tg	286.133	46.2 $^\circ$	47.6 $^\circ$
1.0 Tg	286.12	47.5 $^\circ$	41.6 $^\circ$
Powder	286.29	31.0 $^\circ$	119.6 $^\circ$

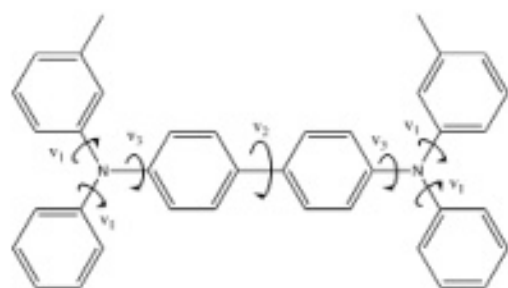
- a. The uncertainty of these dihedral angles is estimated from the uncertainty in the estimate of the offset between experimental and calculated energy scales (50 meV) and the precision of the C-R fits (20 meV):  $\nu_1$  angles are  $\pm 7^\circ$  and  $\nu_2$  angles  $\pm 28^\circ$ . This uncertainty reflects the calibration of the set of angles, and not a unique uncertainty for each angle measurement.

## REFERENCES:

1. S. F. Swallen, K. L. Kearns, M. K. Mapes, Y. S. Kim, R. J. McMahon, M. D. Ediger, T. Wu, L. Yu and S. Satija, *Science* **315** (5810), 353-356 (2007).
2. K. Ishii and H. Nakayama, *Physical Chemistry Chemical Physics* **16** (24), 12073-12092 (2014).
3. I. Lyubimov, M. D. Ediger and J. J. d. Pablo, *The Journal of Chemical Physics* **139** (14), 144505 (2013).
4. S. S. Dalal, A. Sepúlveda, G. K. Pribil, Z. Fakhraai and M. D. Ediger, *The Journal of Chemical Physics* **136** (20), 204501 (2012).
5. K. Ishii, H. Nakayama, S. Hirabayashi and R. Moriyama, *Chem. Phys. Lett.* **459** (1-6), 109-112 (2008).
6. Y. Esaki, T. Komino, T. Matsushima and C. Adachi, *The Journal of Physical Chemistry Letters* **8** (23), 5891-5897 (2017).
7. Y. Qiu, S. S. Dalal and M. D. Ediger, *Soft Matter* **14** (15), 2827-2834 (2018).
8. M. D. Ediger, *The Journal of Chemical Physics* **147** (21), 210901 (2017).
9. C. Rodríguez-Tinoco, M. Gonzalez-Silveira, J. Ràfols-Ribé, A. F. Lopeandía and J. Rodríguez-Viejo, *Physical Chemistry Chemical Physics* **17** (46), 31195-31201 (2015).
10. K. Dawson, L. A. Kopff, L. Zhu, R. J. McMahon, L. Yu, R. Richert and M. D. Ediger, *The Journal of Chemical Physics* **136** (9), 094505 (2012).
11. K. L. Kearns, S. F. Swallen, M. D. Ediger, T. Wu, Y. Sun and L. Yu, *The Journal of Physical Chemistry B* **112** (16), 4934-4942 (2008).
12. S. L. L. M. Ramos, M. Oguni, K. Ishii and H. Nakayama, *The Journal of Physical Chemistry B* **115** (49), 14327-14332 (2011).
13. K. L. Kearns, K. R. Whitaker, M. D. Ediger, H. Huth and C. Schick, *The Journal of Chemical Physics* **133** (1), 014702 (2010).
14. K. J. Dawson, K. L. Kearns, M. D. Ediger, M. J. Sacchetti and G. D. Zografis, *The Journal of Physical Chemistry B* **113** (8), 2422-2427 (2009).
15. M. S. Beasley, M. Tylinski, Y. Z. Chua, C. Schick and M. D. Ediger, *The Journal of Chemical Physics* **148** (17), 174503 (2018).
16. A. Laventure, T. Maris, C. Pellerin and O. Lebel, *Crystal Growth & Design* **17** (5), 2365-2373 (2017).
17. Z. Fakhraai and J. A. Forrest, *Science* **319** (5863), 600-604 (2008).
18. S. S. Dalal and M. D. Ediger, *The Journal of Physical Chemistry Letters* **3** (10), 1229-1233 (2012).
19. D. Yokoyama, A. Sakaguchi, M. Suzuki and C. Adachi, *Applied Physics Letters* **93** (17), 173302 (2008).
20. A. A. Gujral, University of Wisconsin, 2017.
21. S. F. Swallen, K. L. Kearns, S. Satija, K. Traynor, R. J. McMahon and M. D. Ediger, *The Journal of Chemical Physics* **128** (21), 214514 (2008).
22. S. S. Dalal, Z. Fakhraai and M. D. Ediger, *The Journal of Physical Chemistry B* **117** (49), 15415-15425 (2013).
23. S. S. Dalal and M. D. Ediger, *The Journal of Physical Chemistry B* **119** (9), 3875-3882 (2015).
24. S. S. Dalal, D. M. Walters, I. Lyubimov, J. J. de Pablo and M. D. Ediger, *Proceedings of the National Academy of Sciences* **112** (14), 4227-4232 (2015).

25. M. Shibata, Y. Sakai and D. Yokoyama, *Journal of Materials Chemistry C* **3** (42), 11178-11191 (2015).
26. S. S. Dalal, University of Wisconsin - Madison, 2014.
27. O. Dhez, H. Ade and S. G. Urquhart, *Journal of Electron Spectroscopy and Related Phenomena* **128** (1), 85-96 (2003).
28. E. G. Rightor, S. G. Urquhart, A. P. Hitchcock, H. Ade, A. P. Smith, G. E. Mitchell, R. D. Priester, A. Aneja, G. Appel, G. Wilkes and W. E. Lidy, *Macromolecules* **35** (15), 5873-5882 (2002).
29. J. Stöhr and M. G. Samant, *Journal of Electron Spectroscopy and Related Phenomena* **98-99**, 189-207 (1999).
30. S. Banerjee, T. Hemraj-Benny, S. Sambasivan, D. A. Fischer, J. A. Misewich and S. S. Wong, *The Journal of Physical Chemistry B* **109** (17), 8489-8495 (2005).
31. W. Zhang, A. Nefedov, M. Naboka, L. Cao and C. Wöll, *Physical Chemistry Chemical Physics* **14** (29), 10125-10131 (2012).
32. S. D. Perera and S. G. Urquhart, *The Journal of Physical Chemistry A* **121** (26), 4907-4913 (2017).
33. S. G. Urquhart, M. Martinson, S. Eger, V. Murcia, H. Ade and B. A. Collins, *The Journal of Physical Chemistry C* **121** (39), 21720-21728 (2017).
34. C. Bishop, J. L. Thelen, E. Gann, M. F. Toney, L. Yu, D. M. DeLongchamp and M. D. Ediger, *Proceedings of the National Academy of Sciences* **116**, 21421-21426 (2019).
35. J. Wang, G. Cooper, D. Tulumello and A. P. Hitchcock, *The Journal of Physical Chemistry A* **109** (48), 10886-10896 (2005).
36. A. Gujral, K. A. O'Hara, M. F. Toney, M. L. Chabinyk and M. D. Ediger, *Chemistry of Materials* **27** (9), 3341-3348 (2015).
37. K. V. Kaznatcheev, C. Karunakaran, U. D. Lanke, S. G. Urquhart, M. Obst and A. P. Hitchcock, *Nuclear Instruments and Methods in Physics Research Section A: Accelerators, Spectrometers, Detectors and Associated Equipment* **582** (1), 96-99 (2007).
38. Y. Ma, C. T. Chen, G. Meigs, K. Randall and F. Sette, *Physical Review A* **44** (3), 1848-1858 (1991).
39. A. P. Hitchcock and D. C. Mancini, *Journal of Electron Spectroscopy and Related Phenomena* **67** (1), vii (1994).
40. T. Regier, J. Krochak, T. K. Sham, Y. F. Hu, J. Thompson and R. I. R. Blyth, *Nuclear Instruments and Methods in Physics Research Section A: Accelerators, Spectrometers, Detectors and Associated Equipment* **582** (1), 93-95 (2007).
41. A. P. Hitchcock, (McMaster University, ON Canada, 2018).
42. OriginPro, Version 2019, 2019, Northampton, MA, USA
43. SigmaPlot, Version 10.0, 2006, San Jose, CA, USA
44. B. Axelrod, Best Fitting Plane given a Set of Points, 2017, Mathematics Stack Exchange <https://math.stackexchange.com/q/2306029>
45. The notation of "aromatic" in the "carbon 1s  $\rightarrow$   $\pi^*$ <sub>Aromatic</sub> transition" nomenclature is used instead of the traditional "carbon 1s  $\rightarrow$   $\pi^*$ <sub>C=C</sub>" notation, as the latter tends to reinforce an incorrect localized bond interpretation of the electronic transition..
46. M. J. Frisch, G. W. Trucks, H. B. Schlegel, G. E. Scuseria, M. A. Robb, J. R. Cheeseman, G. Scalmani, V. Barone, G. A. Petersson, H. Nakatsuji, X. Li, M. Caricato, A. V. Marenich, J. Bloino, B. G. Janesko, R. Gomperts, B. Mennucci, H. P. Hratchian, J. V. Ortiz, A. F. Izmaylov, J. L. Sonnenberg, Williams, F. Ding, F. Lipparini, F. Egidi, J. Goings, B. Peng, A. Petrone, T.

- Henderson, D. Ranasinghe, V. G. Zakrzewski, J. Gao, N. Rega, G. Zheng, W. Liang, M. Hada, M. Ehara, K. Toyota, R. Fukuda, J. Hasegawa, M. Ishida, T. Nakajima, Y. Honda, O. Kitao, H. Nakai, T. Vreven, K. Throssell, J. A. Montgomery Jr., J. E. Peralta, F. Ogliaro, M. J. Bearpark, J. J. Heyd, E. N. Brothers, K. N. Kudin, V. N. Staroverov, T. A. Keith, R. Kobayashi, J. Normand, K. Raghavachari, A. P. Rendell, J. C. Burant, S. S. Iyengar, J. Tomasi, M. Cossi, J. M. Millam, M. Klene, C. Adamo, R. Cammi, J. W. Ochterski, R. L. Martin, K. Morokuma, O. Farkas, J. B. Foresman and D. J. Fox, Gaussian 16 Rev. C.01, 2016, Wallingford, CT
47. Koster. A.M., Cinvestav, Mexico City 2018 (2018).
48. G. Geudtner, P. Calaminici, J. Carmona-Espíndola, J. M. del Campo, V. D. Domínguez-Soria, R. F. Moreno, G. U. Gamboa, A. Goursot, A. M. Köster, J. U. Reveles, T. Mineva, J. M. Vásquez-Pérez, A. Vela, B. Zúñiga-Gutierrez and D. R. Salahub, *Wiley Interdisciplinary Reviews: Computational Molecular Science* **2** (4), 548-555 (2012).
49. L. Triguero, L. G. M. Pettersson and H. Ågren, *Physical Review B* **58** (12), 8097-8110 (1998).
50. U. Fleischer, W. Kutzelnigg, H.-H. Limbach, G. Martin, M. L. Martin and M. Schindler, *Deuterium and Shift Calculation*. (1991).
51. R. R. Cooney and S. G. Urquhart, *The Journal of Physical Chemistry B* **108** (47), 18185-18191 (2004).
52. S. G. Urquhart, H. Ade, M. Rafailovich, J. S. Sokolov and Y. Zhang, *Chem. Phys. Lett.* **322** (5), 412-418 (2000).
53. Y. Ma, F. Sette, G. Meigs, S. Modesti and C. T. Chen, *Physical Review Letters* **63** (19), 2044-2047 (1989).
54. H. Kaji, T. Yamada, N. Tsukamoto and F. Horii, *Chem. Phys. Lett.* **401** (1), 246-253 (2005).
55. A. R. Kennedy, W. E. Smith, D. R. Tackley, W. I. F. David, K. Shankland, B. Brown and S. J. Teat, *Journal of Materials Chemistry* **12** (2), 168-172 (2002).
56. T. Yamada and H. Kaji, *Journal of Molecular Structure* **927** (1), 82-87 (2009).
57. S. D. Perera, S. Shokatian, J. Wang and S. G. Urquhart, *The Journal of Physical Chemistry A* **122** (49), 9512-9517 (2018).



Scheme 1

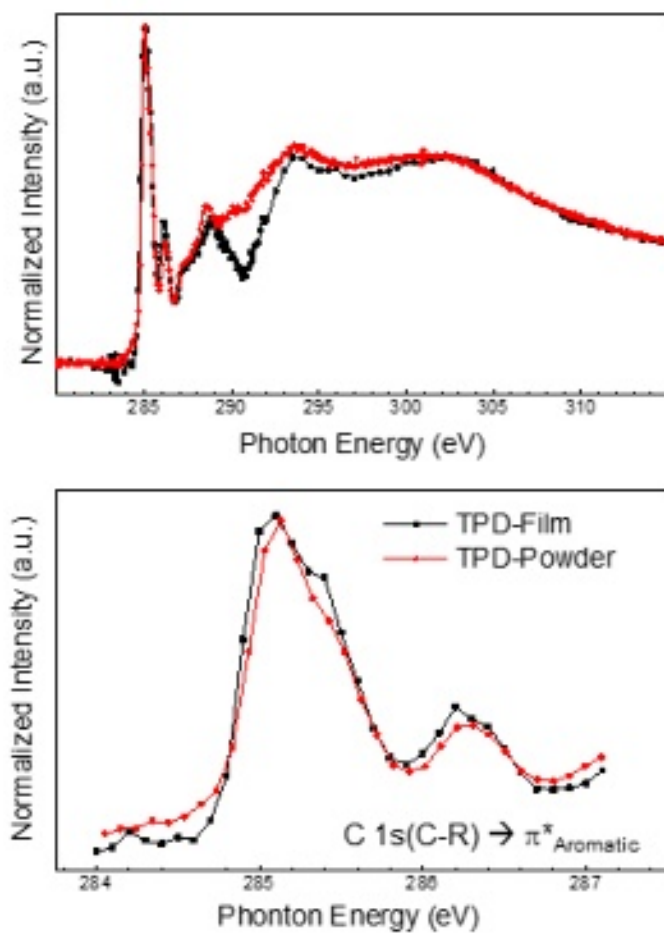


Figure 1

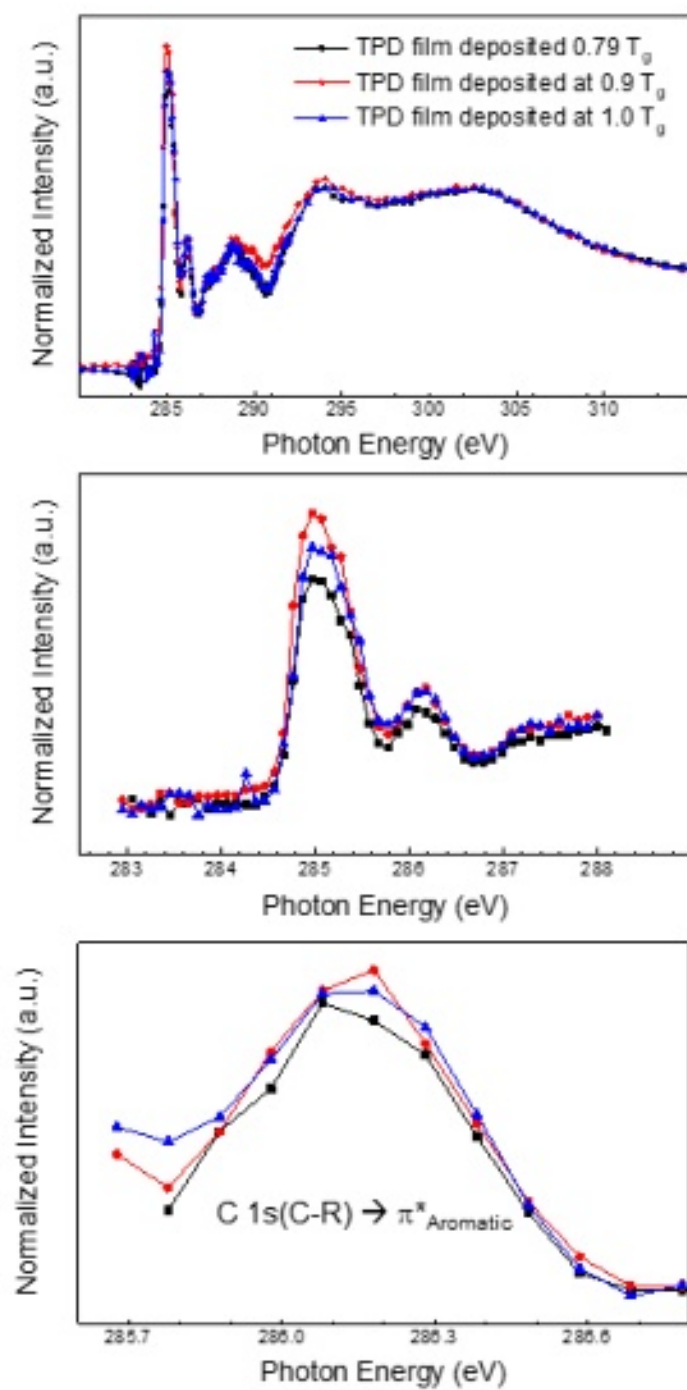


Figure 2



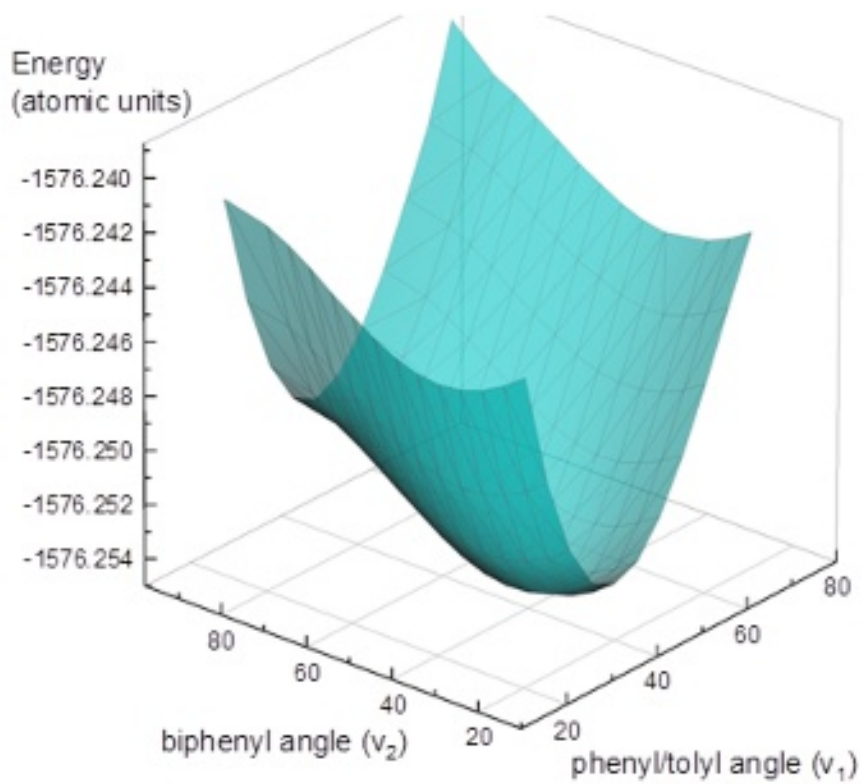


Figure 4

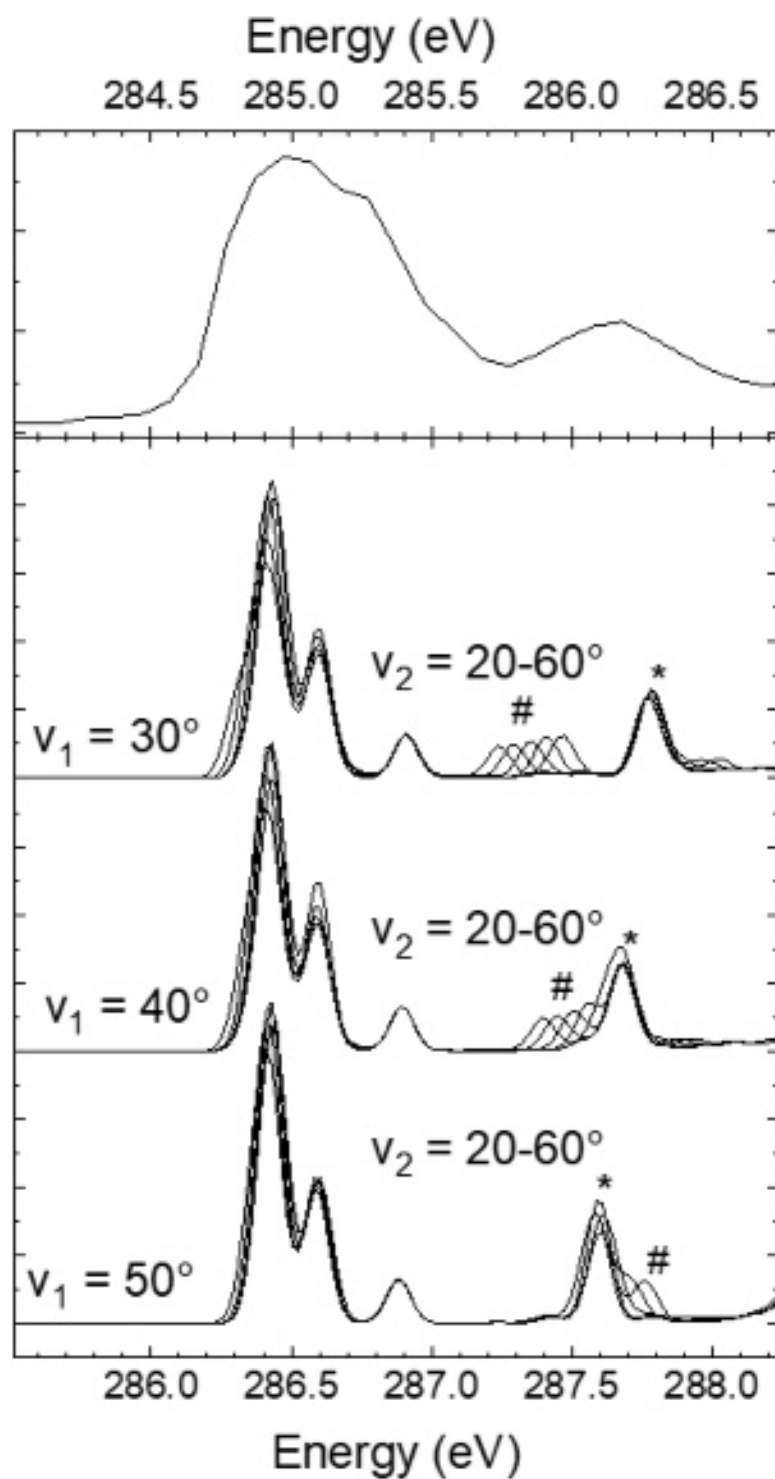


Figure 5

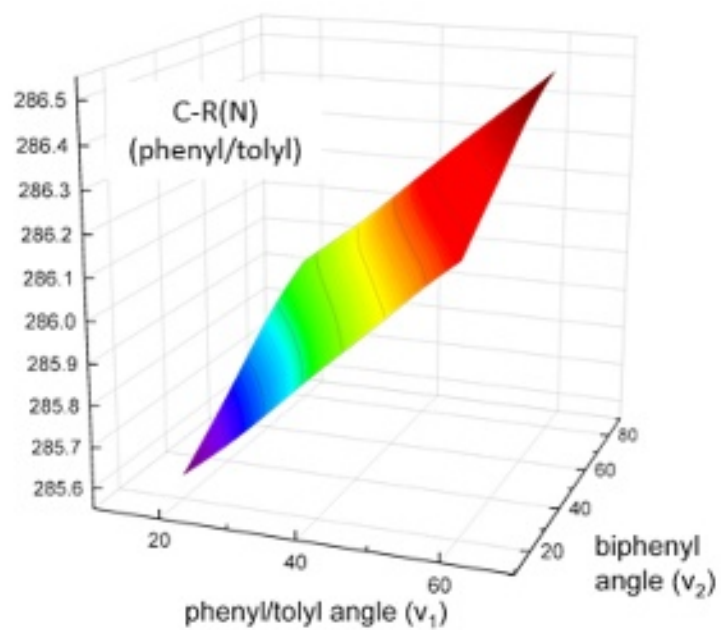
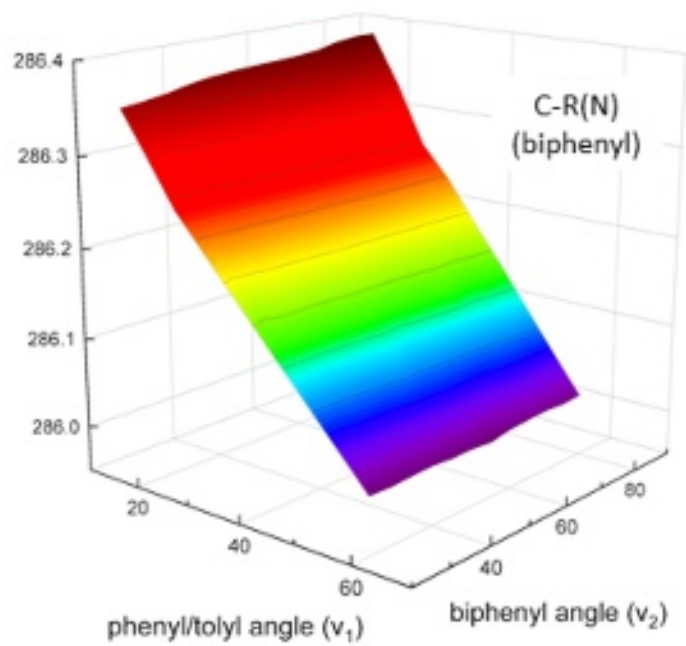


Figure 6